Advanced Intelligent Systems

ADVANCED INTELLIGENT SYSTEMS Open Access

www.advintellsyst.com

RESEARCH ARTICLE OPEN ACCESS

Cellular Material Network: A General Machine Learning Architecture for Predicting Mechanical Properties of Cellular Materials

Sicong Zhou[1] | Qiang Gao[2] | Liuchao Jin[1] | Guoquan Xie[1] | Kang Zhang[1] | Wei-Hsin Liao[1,3]

[1]Department of Mechanical and Automation Engineering, The Chinese University of Hong Kong, Hong Kong, China | [2]School of Mechanical Engineering, Southeast University, Nanjing, China | [3]Institute of Intelligent Design and Manufacturing, The Chinese University of Hong Kong, Hong Kong, China

Correspondence: Wei-Hsin Liao (whliao@cuhk.edu.hk)

Received: 1 April 2026 | **Revised:** 20 July 2026 | **Accepted:** 22 July 2026

Keywords: artificial neural network | cellular metamaterials | energy absorption | physical-informed model | theoretical model

ABSTRACT

Cellular materials with porous and lightweight structures have attracted attention due to exceptional mechanical tunability and broad applications. Despite advancements in design strategies, traditional simulations remain computationally intensive, motivating developments of efficient optimization methodologies. This study introduces Cellular Material Network (CM-Net), a physics-informed machine learning architecture for predicting mechanical properties of cellular materials. By treating basic geometric units as tokens analogous to those in natural language processing, CM-Net achieves efficient forward prediction and generalization across diverse structures and compositions. Validated against simulations and experiments, CM-Net accurately predicts nonlinear behaviors, including initial peak compression force, mean compression force, and energy absorption. The model maintains low relative errors for out-of-distribution scenarios such as varying wall thicknesses and novel topologies composed of short straight segments. However, extrapolation accuracy decreases for geometries with long curved edges, owing to insufficient representation of deformation mechanisms in training. CM-Net also predicts the behavior of composite and gradient structures, as well as nonlinear force–displacement curves. We further demonstrate inverse designs of complex irregular cellular materials to meet specific requirements, illustrating CM-Net's utility as a design assistant, with experimental validation confirming its practical applicability. Its scalability and generalizability make CM-Net a transformative tool for accelerating lightweight, high-performance cellular material development.

1 | Introduction

Cellular materials, consisting of a solid matrix (e.g., metals, polymers, or ceramics) configured in repetitive cellular architectures, represent a category of porous, lightweight structures. Common examples include foams [1, 2], lattices [3–6], and thin-walled structures [7, 8], each exhibiting distinct structural features and broad applications. Their mechanical properties are highly tunable, influenced by both geometric configuration and material composition [9]. Systematically tuning parameters like cell size, wall thickness, and topology enables the precise tailoring of mechanical properties, such as Poisson's ratio [10], stiffness [11], strength [12], energy storage [5] and absorption [8] capacities, deformation coupling [5] and uncoupling [13], thermal resistance [14], and sound damping [15], to meet specific design requirements. The inherent porosity of cellular materials enables substantial mass reduction while preserving structural integrity, thereby optimizing the trade-off between mechanical performance and weight. These characteristics make cellular materials ideal for advanced engineering applications [16, 17], including aerospace and automotive systems requiring improved fuel efficiency and safety, construction with enhanced thermal

insulation, protective packaging, and biomedical tissue engineering. Consequently, research on cellular materials has become a central theme in modern engineering innovation.

Various strategies have been developed to enhance the mechanical performance of cellular materials. Bio-inspired strategies, which draw on evolutionary principles from natural systems, offer innovative approaches to engineering challenges. Examples include curved design [2], gradient design [18], hierarchical design [10], hybrid design [7], and irregular design [19], each providing unique benefits. Curved profiles mitigate stress concentration and reduce fracture risk, combining aesthetic appeal with mechanical robustness. Functionally graded materials address conflicting requirements (e.g., the hardness-toughness trade-offs) and exhibit multi-stage energy absorption (EA) during impact. Hierarchical designs optimize strength-to-weight ratios and improve damage tolerance via multiscale stress redistribution. Hybrid designs exploit the unique properties of diverse materials or structures to achieve precisely tuned mechanical behaviors. Irregular designs harness geometric stochasticity and functional heterogeneity to provide robustness, imperfection tolerance, and adaptive energy dissipation, enabling flexible regulation of structure-performance relationships. Implementing such designs requires substantial engineering expertise and relies on both simulation and experimental validation (Figure 1a). However, experiments are costly, making simulations indispensable for initial design iterations and final optimization. Conventional simulations, however, remain computationally intensive and time-consuming, posing high cost in trial-and-error design workflows.

Given the flourishing development of artificial intelligence, machine learning has emerged as a transformative paradigm in mechanical research [22–26]. Various machine learning models have been constructed for forward prediction [27–29] and inverse design [30–33] (based on forward prediction), enabling the creation of novel cellular materials with exceptional mechanical properties. Notably, artificial neural networks are particularly adept at modeling nonlinear spaces, making them ideal for capturing the nonlinear behaviors of cellular materials. Therefore, models based on diverse architectures, such as random forest regression model [28], multi-layer perceptrons [20, 29–36] (MLPs), convolutional neural networks [37–44] (CNNs, including 2D CNNs [37–41] and 3D CNNs [42–44]), and graph neural networks [45–49] (GNNs), have been developed to predict mechanical properties of cellular materials. However, due to architectural limitations (e.g., inability to handle variable dimensionalities) or representational constraints (e.g., lack of a unified parameterization for arbitrary structures), most of these models lack a generalizable framework for cellular materials. As a result, these models are often confined to limited design spaces (e.g., specific constituent materials or structural configurations), thereby restricting their broader applicability. For instance, pixel- or voxel-based image parameterization for CNNs poses challenges for cellular materials with large arrays, as these approaches typically require extremely high resolutions

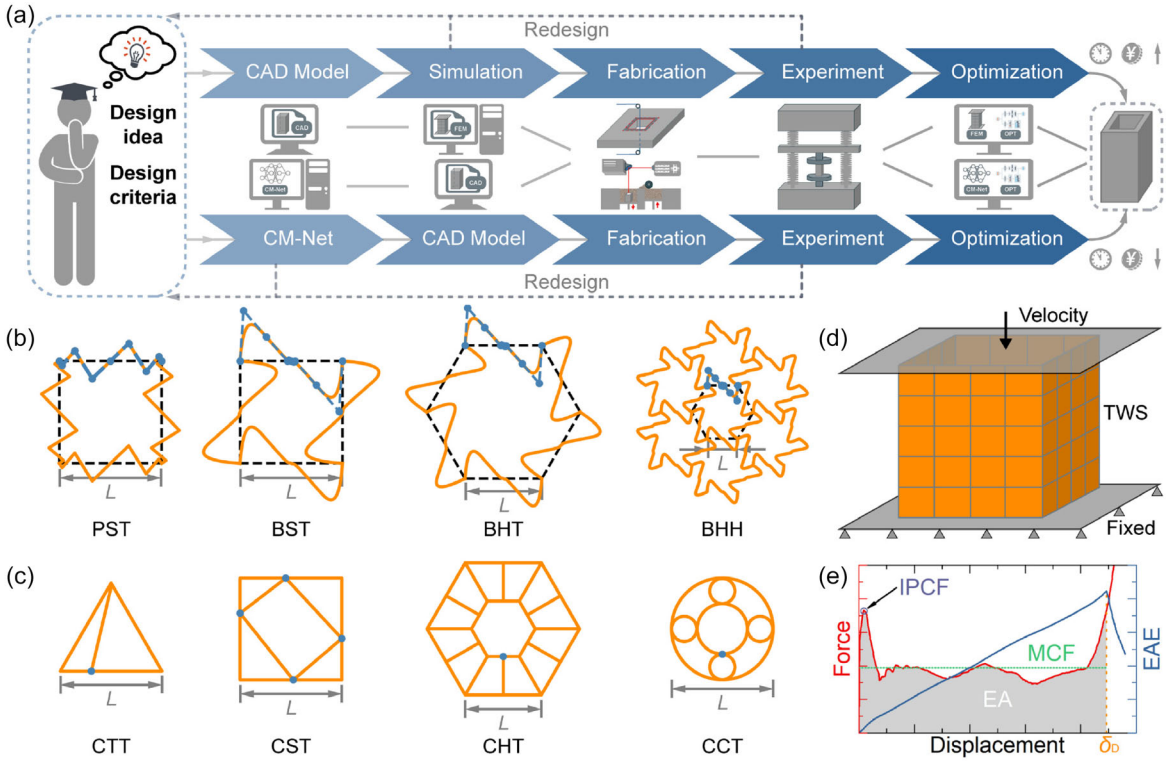

FIGURE 1 | Design and performance evaluation of cellular materials. (a) Traditional design relies on simulations, consuming substantial time and resources. CM-Net enables rapid performance evaluation, reducing iteration cycles. (b) Polyline and curve TWSs are generated using B-spline curves based on fundamental square and hexagonal cross-sectional shapes. (c) Various common TWSs, including triangular, square, hexagonal, and circular forms, are included in the dataset to improve diversity. (d) In the FEM validated by experiments [20, 21], TWSs are compressed between rigid plates at a constant velocity to obtain the quasi-static force–displacement relationship. (e) Energy absorption metrics are calculated from FEM-derived force–displacement curves.

[38, 42]. Graph-based representations are expressive in principle, yet most existing implementations for cellular materials have been restricted to unit-cell-based, regular straight-strut structures [46, 47], a constraint of current practice rather than an inherent shortcoming of graph neural networks. Moreover, many unit-cell-based studies focus on homogenized properties [38, 43, 47] or limited array numbers [28, 42], often ignoring the influence of boundary conditions that are critical in practical applications. Additionally, some models are limited to predicting mechanical properties under small deformations [45–48] (e.g., elastic modulus and compressive strength), which represent relatively simpler problems compared to those involving large nonlinear deformations with complex contact behaviors, such as EA process.

To address these limitations, it is essential to develop generalizable architectures for cellular materials, akin to how natural language processing (NLP) models [50, 51] handle diverse linguistic inputs. In addition, integrating physical information (e.g., energy dissipation mechanisms) can mitigate data-driven biases and ensure that predictions conform to physical principles [52–54], while requiring smaller training set [55–57]. Within a given physical domain, this approach not only enhances model generalizability [53] across diverse conditions but also improves interpretability [57] through domain-relevant variables. We focus on the out-of-plane EA of thin-walled structures (TWSs), such as tubes and honeycombs, which exhibit significant nonlinearity due to plasticity, buckling, and frictional contact. This serves as a representative case study for developing our proposed Cellular Material Network (CM-Net) framework. Implementing this approach requires an efficient design-property mapping to serve as training data for CM-Net. A detailed description of the key concepts and model architecture is provided in the subsequent sections.

2 | Design of CM-Net

2.1 | Generation of Thin-Walled Structures With Diverse Topology

To train CM-Net effectively, a comprehensive dataset of paired mechanical designs and their corresponding nonlinear mechanical properties is required. We employ B-spline curves to construct the edges of TWSs, thereby significantly expanding the design space. Based on conventional square and hexagonal cross-sectional shapes, we generated three distinct types of structures (Figure 1b): B-spline square tubes (BSTs), B-spline hexagonal tubes (BHTs), and B-spline hexagonal honeycombs (BHHs). These structures enabled CM-Net to learn the influence of included angles on EA performance and the EA capabilities of curved-edge TWSs. Additionally, polyline square tubes (PSTs, Figure 1b) were designed to facilitate understanding of the EA characteristics of 2-segment folding elements (fundamental building blocks in most designs) and straight-edged TWSs. To further enhance the topological diversity of the training set, we included a variety of common TWSs based on triangular, square, hexagonal, and circular cross-sectional shapes (Figure 1c; detailed in Figure S1). The control points (blue points in Figure 1b) of B-spline curves and polylines are both randomly generated under disjoint constraints. The wall thicknesses of TWSs are also randomized to introduce variability into the training set. Finite element models (FEM) are used to simulate quasi-static compression processes, during which samples are sandwiched between two rigid plates (Figure 1d, one plate moves at a specified compression velocity in the vertical direction, while the other is fully fixed). Frictional contact and experimentally validated elastoplastic material models ensure realistic simulation outcomes. Using this framework, we generated 30 563 unique design-performance pairs, encompassing initial peak compression force (IPCF), mean compression force (MCF), and EA metrics (Figure 1e). Detailed simulation parameters and definition of the EA metrics are provided in the Methods.

2.2 | Physical Information for CM-Net

Over the past few decades, advancements in plasticity mechanics have established several methods for analyzing the EA performance of TWSs. Among these, the super folding element theory, an analysis method based on energy balance, has become the most commonly used approach for calculating the MCF of TWSs undergoing progressive folding deformation [21, 58]. While this method demonstrates strong predictive capabilities for straight-edged TWSs, its accuracy diminishes when applied to structures with curved edges [59]. To address this limitation, we developed a unified theoretical model capable of predicting MCF for both straight- and curved-edge TWSs under the same loading conditions. The derived formula is expressed as

$$\mathrm{MCF_P} = \frac{1}{4\cdot \mathrm{CDE_P}}\sqrt{\frac{\sigma_y\sigma_h}{n+1}}t^{1.5}\left(\sqrt{2\pi\Lambda_{\mathrm{PB}}\Gamma_{\mathrm{PM}}}+\frac{1}{2}(\Omega_{\mathrm{PB}}+2\mathrm{K_{PR}})\sqrt{t}\right) \tag{1}$$

where σ_y, σ_h, n, t, $\mathrm{CDE_P}$, Λ_{PB}, Ω_{PB}, Γ_{PM}, and $\mathrm{K_{PR}}$ are yield stress, hardening stress, power law exponent, wall thickness, compression displacement efficiency, primary bending energy, secondary bending energy, membrane energy, and rolling energy coefficient for progressive folding deformation, respectively. However, compressed TWSs may also experience global buckling, which typically results in lower MCF compared to progressive folding. To account for this alternative deformation mode, we developed a complementary theoretical model specifically for predicting MCF under global buckling conditions, expressed as

$$\mathrm{MCF_G} = \frac{1}{8\cdot \mathrm{CDE_G}}\sqrt{\frac{\sigma_y\sigma_h}{n+1}}t^{2}\left(\frac{\pi\Lambda_{\mathrm{GB}}}{H'}+\frac{\Omega_{\mathrm{GB}}}{H'}+\frac{\Gamma_{\mathrm{GM}}}{H't}+2\mathrm{K_{GR}}\right) \tag{2}$$

where $\mathrm{CDE_G}$, Λ_{GB}, Ω_{GB}, Γ_{GM}, and $\mathrm{K_{GR}}$ are compression displacement efficiency, primary bending energy, secondary bending energy, membrane energy, and rolling energy coefficient for global buckling deformation, respectively, and H' is half of the height of TWS. A third scenario, a mixed deformation mode involving both progressive folding ($\mathrm{MCF_P}$) and global buckling ($\mathrm{MCF_G}$) mechanisms, can also occur. In such cases, MCF is calculated as

$$\mathrm{MCF} = \alpha\cdot\mathrm{MCF_P}+\beta\cdot\mathrm{MCF_G} \tag{3}$$

where α and β represent the proportional contributions of progressive folding and global buckling modes, respectively, with $\alpha + \beta = 1$. This comprehensive framework enables accurate

prediction of MCF for TWSs subjected to arbitrary deformation modes. Detailed derivations are provided in Section S2. These physical information equations were used to construct the corresponding physical information layer in CM-Net (details in Section S3.2). By merging this physical information, the extrapolation capacity of CM-Net can be significantly improved (details in Section S5.1).

2.3 | General Architecture of CM-Net

Several key principles guide the design of general machine learning models. The first is transferability, enabling a model to adapt to diverse tasks and datasets without substantial modification. The second is scalability, allowing integration of new features and handling increasingly complex tasks. The third is data efficiency, ensuring effective learning from limited training data. NLP models such as ChatGPT-4 [50] and DeepSeek-R1 [51] exemplify these principles, processing language through token-based representations, basic units that form meaningful sentences. Disrupting token sequences often eliminates meaning, whereas different ordered sequences yield distinct interpretations (Figure 2a). Inspired by this approach, we propose CM-Net, a general machine learning architecture for predicting the mechanical properties of cellular materials. It is important to clarify that while we draw inspiration from the token-based representation in NLP, the order-invariance of CM-Net aligns it more closely with permutation-invariant architectures such

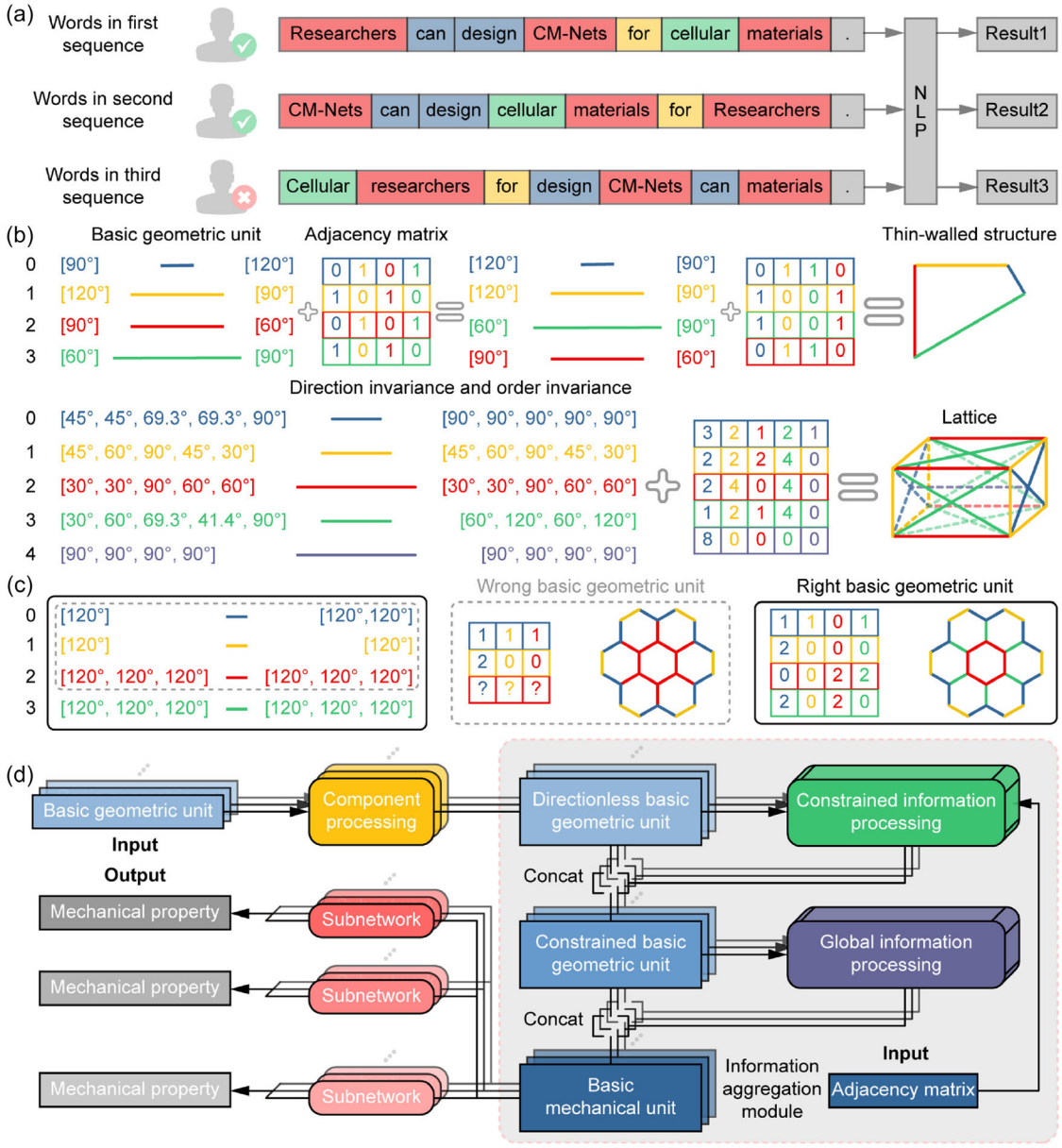

FIGURE 2 | Design concept and architecture of CM-Net. (a) In NLPs, words form the basic units of language, and their order influences the meaning of the whole sentence. (b) Cellular materials are represented by geometric units and their connection relationships through an adjacency matrix. These units are order- and direction-invariant, allowing flexible arrangements. (c) Each basic geometric unit must maintain consistent connection relationships, such as identical adjacent panels, rather than merely sharing the same constrained angles. (d) CM-Net's architecture includes a component processing module, an information aggregation module, and a mechanical property prediction module with multiple subnetworks.

as Deep Sets [60], PointNet [61], and Set Transformers [62]. Unlike general set models, however, CM-Net incorporates architectural elements derived from mechanical mechanisms.

To achieve generality, CM-Net processes inputs, basic geometric units, analogous to NLP tokens, with the critical distinction that prediction outcomes remain invariant to the ordering of tokens in the input. For example, the basic geometric units for TWSs, strut-based lattices, and plate-based lattices correspond respectively to panels (which degenerate into edges, Figure 2b), struts (degenerating into profiles, Figure 2b), and plates. Notably, the same basic geometric unit maintains consistent connection relationships (Figure 2c), since the mechanical properties vary under different constraints. Thus, a basic mechanical unit comprises a basic geometric unit, boundary conditions, and global characteristics; overall structural properties emerge through the aggregation of constituent basic mechanical units. To capture boundary conditions, we employ an adjacency matrix that symmetrically or asymmetrically represents structural connectivity, depending on the structural symmetry (Figure 2b–c). The basic geometric unit for TWSs is characterized by the number of repeated units, point coordinates, wall thickness, included angles between intersecting panels, and material parameters (Figure S10).

CM-Net's inputs comprise all basic geometric units within a cellular material and the corresponding adjacency matrix (Figure 2d). Each unit is processed through identical neural networks, allowing CM-Net to handle cellular materials with arbitrary numbers of basic geometric units. In the component processing module, basic geometric units are first split into several components. The directional nature of these units (e.g., differing included angles at each end) necessitates operations in this module to ensure that predictions are independent of direction. In addition, to maintain independence from the number of included angles, they are processed through identical neural layers followed by sum aggregation. The component processing module yields directionless geometric information for the information aggregation module. The adjacency matrix, which is crucial for extracting constraint and connectivity information, enables the formation of constrained basic geometric units. The multi-head self-attention mechanism, a strategy successful in NLP and computer vision tasks, is applied in the global information processing module to capture structural global characteristics. Based on these foundations, subnetworks in the mechanical property prediction module can predict different mechanical properties of the cellular material from the basic mechanical units. Importantly, linear layers lack biases to avoid potential influence of zero-padding on prediction results. Full implementation details of CM-Net specific to TWSs are provided in the Methods, Sections S3 and S4, and the Code availability.

3 | Performance of CM-Net

3.1 | Interpolation and Extrapolation Capabilities of CM-Net

The architecture of CM-Net integrates mechanical decomposition principles with physics-informed neural networks, enhancing the reliability and interpretability of its predictions. Our primary contribution lies in demonstrating that CM-Net excels at predicting designs both within (interpolation) and outside (extrapolation) the training space. We evaluated the interpolation performance of CM-Net on 1600 randomly generated unseen test cases within the training domain. The network demonstrated superior accuracy, particularly for the prediction of IPCF, with an average relative error of only 2.92%. This high precision arises because the absence of contact during the initial stage simplifies load-bearing and deformation complexity. Therefore, CM-Net is expected to be well-suited for predicting elastic mechanical properties such as elastic modulus and elastic limit. For MCF and EA, CM-Net also achieved excellent performance, with average relative errors of 11.72% and 10.80%, respectively. These results are sufficient to guide preliminary engineering design decisions. The agreement between predicted and high-fidelity FEM responses confirms the accurate estimation of EA capabilities in TWSs with diverse cross-sectional shapes, constituent materials, and deformation modes (Figure 3). Generally, CM-Net exhibits the best prediction performance for BHHs compared to PSTs, BSTs, and BHTs (detailed in Table S4), due to relatively stable deformation of BHHs caused by strong boundary constraints on the inner panels. This also explains why many TWSs with complex cross-sectional shapes, such as TWSs designed based on hierarchical strategy [21], exhibit similar behavior.

To evaluate CM-Net's generalizability beyond its training domain, a crucial aspect for developing a robust universal model, we conducted extensive tests using samples outside the original design space. These tests included structures with increased wall thickness (1.0–2.0 mm), extended basic lengths ($2L$), novel topological configurations (e.g., polyline hexagonal tubes, PHTs), and materials not encountered during training (AA6061-T4). Although extrapolation performance showed a slight decline compared to interpolation tasks, CM-Net maintained its strongest performance in IPCF prediction across all tested conditions. When evaluating samples with wall thickness exceeding the maximum value (1.0 mm) observed in the training set (Figure 4a), CM-Net exhibited superior performance on diverse topological configurations. However, challenges emerged when predicting properties for samples with significantly extended basic lengths (2x beyond the training set, Figure 4b), particularly for TWSs featuring curved edges. For these cases, the model exhibited relatively large prediction errors (average relative errors of 38.03%, 33.10%, and 35.60% for IPCF, MCF, and EA, respectively) across 40 randomly generated test samples, including BSTs and BHTs. Despite this limitation, CM-Net demonstrated strong performance for TWSs composed of several straight edges (e.g., PSTs). Here, the model achieved average relative errors of 6.67%, 8.72%, and 8.17% across 20 randomly generated test samples for IPCF, MCF, and EA, respectively. This differential performance can be attributed to how CM-Net processes edges: curved edges are treated as single entities, whereas polyline edges are subdivided into smaller segments resembling those encountered during training. Additionally, edge length significantly affects plastic deformation areas, a factor that appears to limit the model's ability to handle long curved edges effectively (relevant knowledge cannot be fully learned from the training set; details in Section S5.1). This suggests the need for targeted augmentation of the training dataset with samples featuring such geometries. When combined with data augmentation and self-similar transformation, CM-Net can

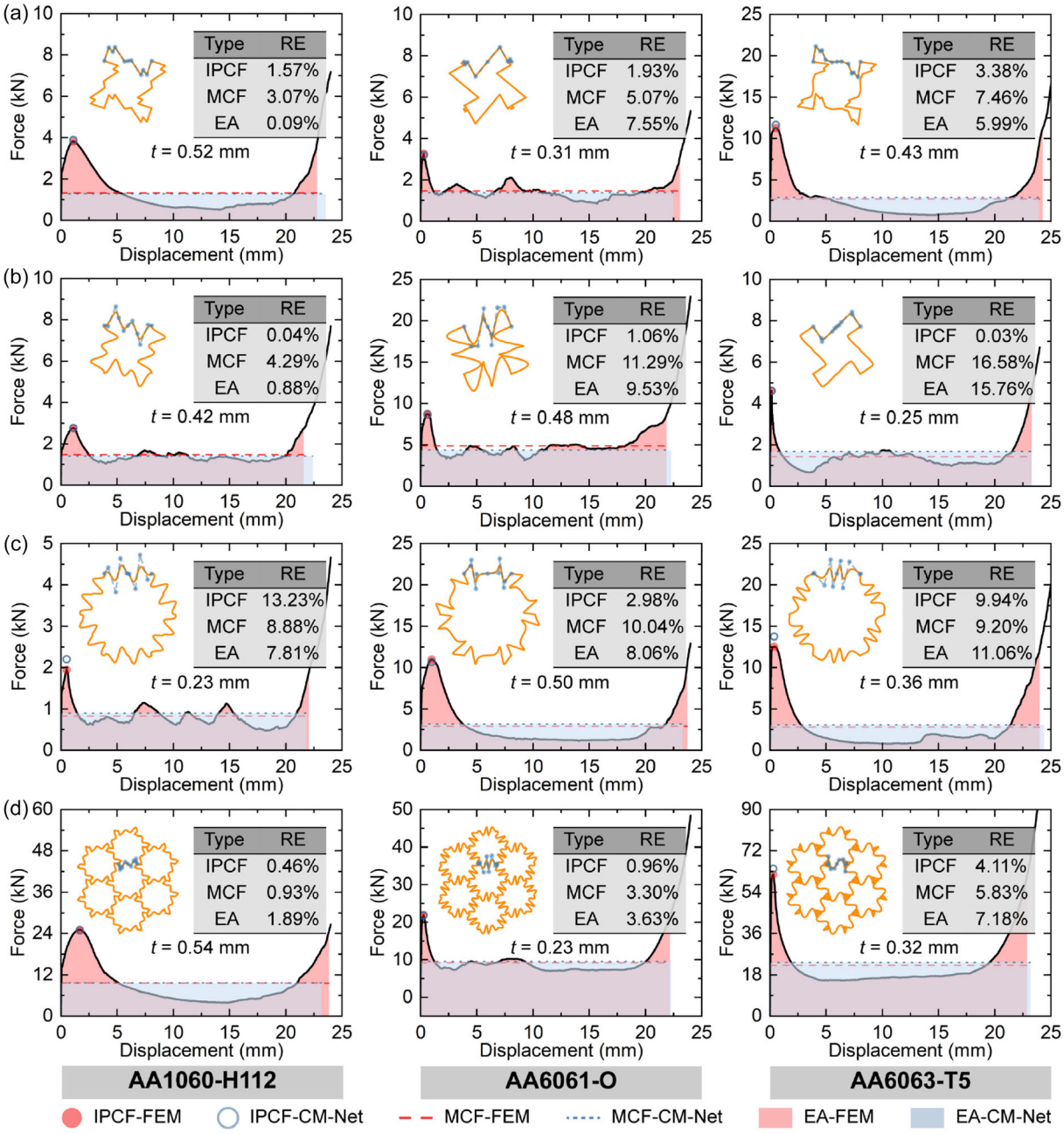

FIGURE 3 | Interpolation ability of CM-Net on representative samples. (a–d) Energy absorption performances of thin-walled structures with different configuration but same design space compared to that in training set are evaluated by CM-Net, considering PSTs in (a), BSTs in (b), BHTs in (c) and BHHs in (d). Each sample is composed of one of three materials, AA1060-H112, AA6061-O, or AA6063-T5. The ground truth values for IPCF, MCF, and EA are derived from the force–displacement curve obtained by FEM, while relative errors (RE) accessed prediction accuracy. Notably, BSTs and BHHs made of AA6061-O and AA6063-T5 were not present in the training set.

predict mechanical performance of TWSs with arbitrary dimensions (Section S1.4 and Figure S15d). CM-Net displayed remarkable robustness when tested on entirely novel topological configurations (Figure 4c), including PHTs, pentagon tubes with reinforcing ribs, and vertex-based hierarchical multi-cell square tubes. Furthermore, the model demonstrated exceptional performance when challenged with samples that simultaneously featured unseen topologies, wall thicknesses, and constituent materials (Figure 4d). These results collectively highlight CM-Net's outstanding versatility and its ability to generalize beyond its training experiences. Details of the interpolation and extrapolation capacities of CM-Net can be found in Section S5.1. Importantly, CM-Net predictions were also compared with experimental results and showed strong agreement, indicating substantial application value (Section S5.2). To further assess the effectiveness of CM-Net, we benchmarked it against several representative baseline models using the same training, validation, and test sets. These baselines include a standard MLP that flattens all input tokens into a fixed vector, a vanilla GNN with simple graph convolutions, a CNN operating on rasterized cross-sectional images, and the forward module of GraphMetaMat [63] (a state-of-the-art graph architecture for 3D truss metamaterials). While all baselines exhibit limited accuracy on extrapolation tasks, CM-Net consistently achieves the lowest prediction errors

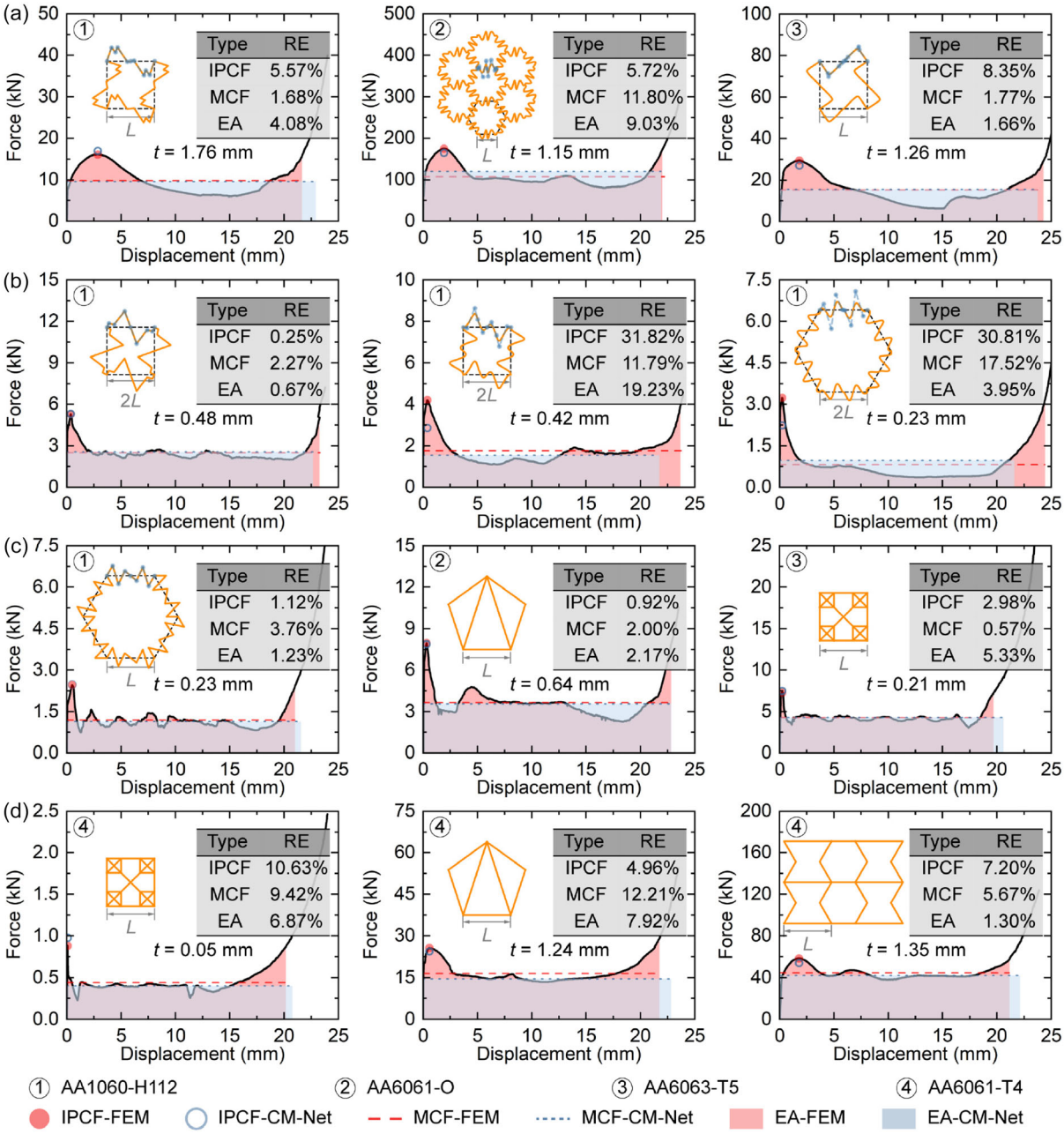

FIGURE 4 | Extrapolation performance of CM-Net on representative samples. (a–d) Energy absorption performances of TWSs outside the design space, considering wall thickness (t) exceeding the maximum value in the training set (1.0 mm) in (a), basic edge length (L) extended beyond the training set by a factor of 2 in (b), novel topologies not encountered during training in (c), and concurrent variations in topology, wall thickness, and constituent material (AA6061-T4) in (d). Each sample is composed of one of four aluminum alloys: AA1060-H112, AA6061-O, AA6063-T5, or AA6061-T4. Notably, the unseen topologies tested include polyline hexagonal tubes, vertex-based hierarchical multi-cell square tubes, and hybrid re-entrant & hexagonal honeycomb structures. To adequately evaluate CM-Net's ability to generalize across novel structural designs, all configurations in test sets were never seen in the training data.

across both interpolation and extrapolation test sets (Table S15). Comprehensive benchmark details are available in Section S7.

3.2 | The Expansion Capability of CM-Net

Composite structures, characterized by the synergistic integration of heterogeneous materials or geometric configurations, demonstrate superior engineering performance through optimized load-bearing capacity and functional adaptability. Leveraging the unique architectural characteristics of CM-Net, this model shows significant potential for predicting the mechanical behavior of TWSs composed of panels with divergent constituent materials and wall thickness distributions. To demonstrate these capabilities, we examined the performance of CM-Net on vertex-based hierarchical multi-cell square tubes, where outer and inner structural components can independently vary in material composition and wall thickness. CM-Net achieves superior prediction accuracy for structures composed of diverse material combinations, effectively capturing the influence of multi-material interactions (Figure 5a). Furthermore, TWSs often feature varying wall thicknesses to optimize EA properties.

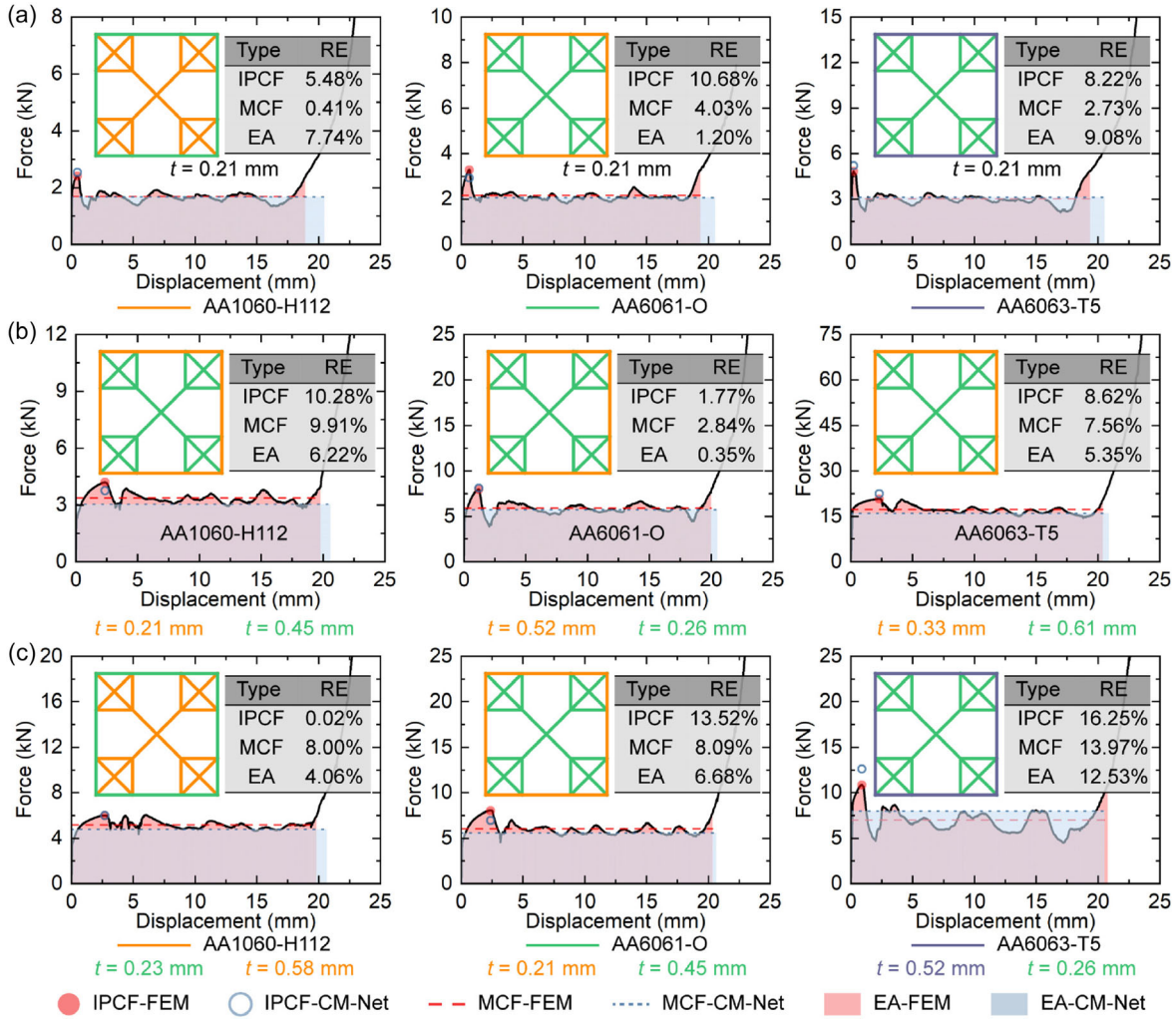

FIGURE 5 | Prediction capacity of CM-Net on composite structures with multi-material and/or varying wall thickness designs. (a–c) Energy absorption performance of thin-walled composite structures for estimating the expansion ability of CM-Net, considering multi-material configurations in (a), wall thickness variations across structural panels in (b), and simultaneous material and wall thickness distribution in (c). Color coding consistently maps to component material and wall thickness composition.

CM-Net robustly handles wall thickness variations between adjacent panels, with the largest observed prediction error being 10.28% (Figure 5b). Importantly, the model also demonstrates robust performance when simultaneously modeling the effects of both constituent materials and varying wall thicknesses (Figure 5c), offering valuable insights for optimization design. As a versatile machine learning architecture, CM-Net achieves high accuracy across different structural configurations, providing practical guidance for design. By adjusting material assignments and thickness distributions, engineers can rapidly identify optimal composite configurations using CM-Net, avoiding costly trial-and-error simulations and experiments.

The modular architecture of CM-Net enables the prediction of force–displacement curves through a specially designed subnetwork within the mechanical property prediction module. Unlike truss-based lattices, which exhibit relatively uniform force–displacement behavior during compression [63], TWSs demonstrate distinct fluctuations in their curves during the buckling phase under out-of-plane compression. These fluctuations are governed by complex interactions between deformation modes and folding wavelengths, which are controlled by geometric and material parameters. The sensitivity of force–displacement characteristics to such parameters presents a significant challenge for high-accuracy prediction, as minor geometric or material variations can drastically alter curve morphology. To address this, we incorporate a discrete Fourier transform within the subnetwork to extract dominant frequency-domain features from force–displacement curves, thereby improving the model's ability to capture morphological complexity. Detailed subnetwork architecture and a comparison with direct time-domain prediction are described in Section S5.4. To evaluate CM-Net's generalization capability, the best-performing model on the validation set was tested on interpolation and extrapolation datasets (Figure 6a). Normalized mean absolute error (NMAE) was adopted as the loss function, reflecting relative discrepancies between predicted and actual values. The distribution of NMAE values across both test sets follows a lognormal distribution (Figure 6b–c), indicating consistent predictive performance. Notably, 93.6% of samples in the interpolation test set and 83.5% in the extrapolation test set achieve NMAE below 15%, demonstrating robustness under both in-domain and out-of-domain conditions. The model exhibits

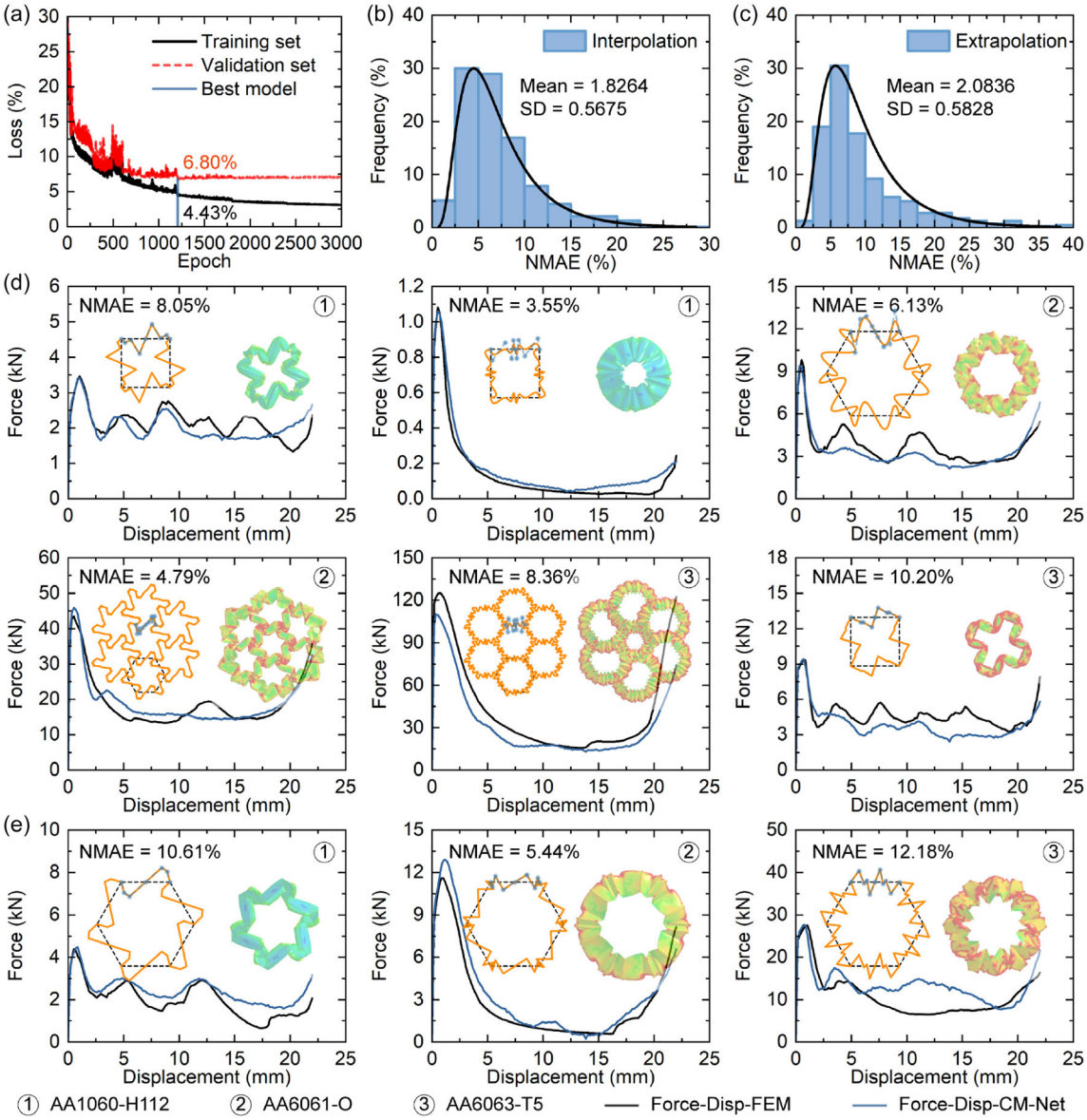

FIGURE 6 | Expansion capacity of CM-Net in predicting force–displacement curves of TWSs. (a) Training process of CM-Net for compression force prediction. (b–c) Distribution of normalized mean absolute error (NMAE) across interpolation and extrapolation test sets, respectively. Black lines represented distribution curves fitted by the lognormal probability density function. (d) Representative samples from the interpolation test set illustrating the CM-Net's predictive accuracy. These samples encompass diverse configuration characteristics, constituted materials, and deformation modes. (e) Representative samples from the extrapolation test set showcasing the CM-Net's predictive performance for polyline hexagonal configurations, which were entirely absent during the training process.

exceptional accuracy in predicting force–displacement curves during the elastic regime (Figure 6d–e), with prediction errors predominantly concentrated in the buckling stage (Table S13). This discrepancy arises from two primary sources: (1) fluctuating misalignment in prediction, and (2) numerical precision errors in force estimation. Despite these challenges, CM-Net successfully captures the overall trends of progressive folding, global buckling, and mixed folding modes, providing a valuable tool for structural deformation mode evaluation. This capability is particularly significant given the complexity of TWS deformation mechanisms. Moreover, CM-Net enables the prediction of force–displacement curves under very large strain (up to 78.6%), which is significantly higher than reported in previous studies [36, 63, 64]. This level of performance underscores the model's robustness and adaptability to complex deformation scenarios, which are critical in applications such as EA and impact resistance. In conclusion, CM-Net demonstrates strong generality, with the potential to be easily adapted to a wide range of prediction tasks and structural configurations. Its high accuracy, coupled with its ability to generalize across diverse design parameters, renders it a powerful tool for engineering design and analysis.

4 | Application of CM-Net in Engineering Design

CM-Net enables powerful and efficient design of cellular materials across diverse design boundaries. To address complex design challenges, disordered architectures constructed using Voronoi

diagram [65] were investigated (Figure 7a). Voronoi diagrams are defined by seed matrices and boundary information, which are systematically translated into input formats compatible with the CM-Net. A small dataset comprising 330 randomly generated samples featuring square, C-, U-, H-, and K-shaped boundaries was used to fine-tune CM-Net for disordered configurations. The fine-tuned CM-Net was then integrated with an optimization algorithm to achieve structures meeting specific design targets (Figure 7b). Initial training and validation losses were 6.5% and 4.7%, respectively, decreasing to 1.2% and 1.0% after fine-tuning (Figure 7c). For EA applications, the maximum IPCF and MCF must be carefully controlled to prevent damage to protected objects. Thus, the design targets focused on maximizing SEA while keeping the IPCF and MCF below 15 kN. Additional manufacturability constraints were incorporated, such as a minimum edge length of 2.0 mm for wire-cut electrical discharge

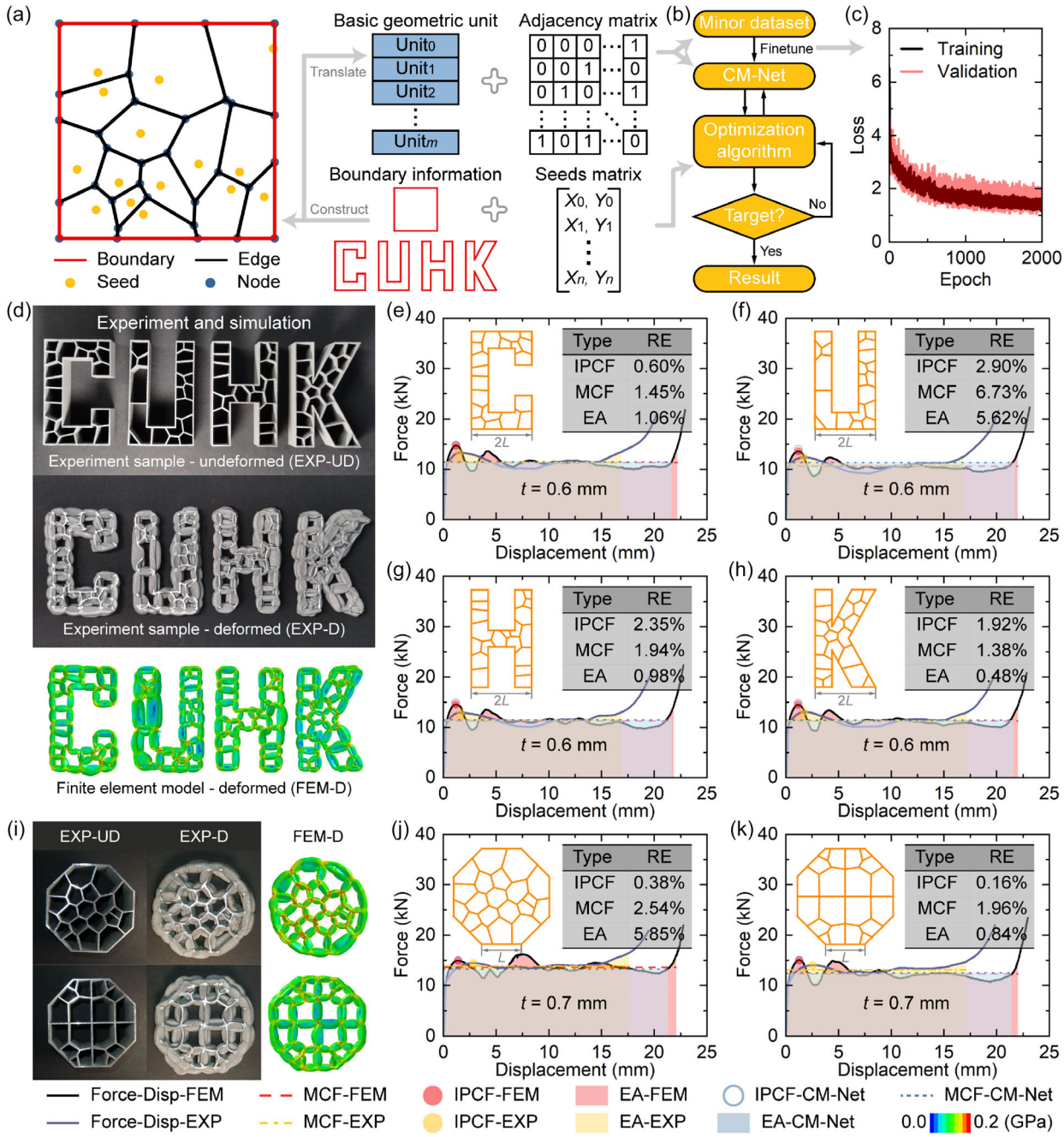

FIGURE 7 | Application of CM-Net in designing disorder multi-cell structures with specific performance targets. (a) Voronoi diagrams are used to generate disorder thin-walled structures based on boundary geometry and seed coordinates. These structures are converted into geometric units and adjacency matrices for CM-Net input. (b) A small training dataset consisting of 231 samples, featuring a variety of boundary shapes (square, C-, U-, H-, and K-shaped), was used for fine-tuning the performance of the CM-Net on Voronoi structures. Structures fulfilling specific design targets were then obtained through an optimization algorithm. (c) Loss–epoch curve during the fine-tuning process. (d–h) Deformation states and EA performance of Voronoi structure with C-, U-, H-, and K-shaped boundaries obtained from quasi-static experiments, simulations, and the CM-Net. (i–k) Similar results for octagonal boundary structures, which were not included in the training set.

machining. Symmetry constraints were also applied to ensure the production of symmetrically optimized structures. Details of the fine-tuning process and optimization algorithm are provided in the Methods. Using this workflow, Voronoi structures with distinct boundary geometries but identical design targets were successfully generated (Figure 7d,i). FEM accurately captured the deformation modes of these structures, as well as the IPCF and MCF. However, FEM tends to overestimate densification displacement due to limitations in the contact algorithms of shell elements [20], particularly for thicker panels and complex configurations. Consequently, CM-Net, being trained on FEM-derived datasets, inherits this systematic overestimation. While the CM-Net predictions showed high consistency with FEM results (relative errors ranging from 0.16% to 6.73%; Figure 7e–h and Figure 7j–k), the relative errors for densification displacement between CM-Net and experiments range from 4.50% to 29.41% (Table S8). This discrepancy significantly influences the absolute accuracy of EA predictions. Therefore, similar to conventional FEM practice, CM-Net serves as a tool for rapid design iteration and relative ranking rather than a replacement for final experimental validation (Figure 1a). Potential solutions in future work are training CM-Net on the dataset collected from experiments or calibrating the densification displacement using a relatively small experimental dataset. Overall, CM-Net demonstrates exceptional promise for engineering applications, enabling significant reductions in design costs while maintaining high predictive accuracy. Its integration with optimization strategies, manufacturability constraints, and symmetry control highlights its versatility in addressing real-world structural design challenges with complex performance requirements.

5 | Discussions and Conclusions

Cellular materials are valued for their exceptional mechanical tunability and lightweight design. However, developing general prediction models for cellular materials poses significant challenges due to the nonlinear and highly complex interactions between diverse geometric configurations, material behaviors, and contact mechanics. Traditional machine learning models, which often rely on limited design spaces and simple property predictions, struggle to capture the intricate nonlinear responses arising from phenomena such as buckling, plastic deformation, and frictional contact during EA. These challenges are particularly acute in TWSs, where out-of-plane compression induces complex deformation mode transitions and fluctuating force–displacement curves. Our proposed CM-Net addresses these limitations by integrating physical principles into a generalizable machine learning framework, enabling efficient forward prediction and robust extrapolation across diverse structural configurations and material compositions.

The core innovation of CM-Net lies in its token-like processing of basic geometric units, inspired by NLP architecture, which enables CM-Net to process cellular materials in a manner analogous to parsing text in NLP systems. This design allows CM-Net to handle both ordered and disordered cellular materials, including TWSs, strut-based lattices, and plate-based lattices, by encoding structural elements into direction-invariant, order-invariant geometric units. This approach not only overcomes the dimensional and topological constraints of previous models (such as CNNs [44] and GNNs [46, 47, 63]) but also enables efficient aggregation of structural information through adjacency matrices and global self-attention mechanisms. Critically, the integration of physically informed energy dissipation principles enhances the model's extrapolation capacity, ensuring that predictions align with physical mechanisms even for out-of-distribution cases. CM-Net's performance, validated through rigorous simulation and experimental comparisons, demonstrates its superiority in both interpolation and extrapolation tasks (Section S5.1 and S5.2). For instance, the model achieves a relative error of only 2.92% for IPCF during interpolation, along with excellent accuracy for nonlinear metrics such as MCF and EA. Notably, its extrapolation capability extends beyond the training domain to scenarios involving multi-material TWSs, extended wall thicknesses, and novel topologies assembled from short straight segments, where it maintains reasonable accuracy. Conversely, the model's efficacy is reduced for structures with long curved edges, where the underlying deformation mechanisms differ significantly from those in the training data (see Section S5.1). In addition to its predictive accuracy, CM-Net's lightweight architecture is capable of reducing computational costs by several orders of magnitude compared to FEM (Section S3.3), enabling rapid design iteration and inverse optimization. Moreover, CM-Net can also be a base model for researchers to fine tune on their own dataset for better local prediction performance. We have shown how CM-Net can be used to design optimal architectures that maximize SEA under the constraints of IPCF and MCF.

Despite these advancements, the current implementation of CM-Net is confined to TWSs and metallic materials, with training data limited to specific boundary conditions and loading scenarios. While this represents a practical starting point, the framework's modular design allows straightforward extension to other cellular structures (e.g., foams, lattices) and diverse materials (e.g., polymers, composites) through additional training data and refinement of physical information layers. Furthermore, expanding the prediction targets (e.g., elastic modulus, Poisson's ratio, or thermal resistance) would require fine-tuning the mechanical property prediction module of CM-Net. The input format, however, remains consistent as a token-based representation of structural elements, preserving generalizability across geometries (e.g., struts for strut-based lattices, plates for plate-based lattices, and void cells for foams).

Looking ahead, several promising directions emerge for the development of CM-Net. First, the integration of a mixture-of-experts (MOE) framework [66] could enable the creation of a large-scale model that synthesizes sub-CM-Nets specialized for distinct structural, material, and boundary types, significantly enhancing predictive accuracy and scalability. Second, extending the model to dynamic loading scenarios or multiscale simulations, such as coupled mechanical-thermal analyses, could unlock new applications in advanced engineering systems. Finally, the fusion of CM-Net with heuristic algorithms [20, 31] or generative models (e.g., GANs [37] or VAEs [30, 46]) could revolutionize the automatic generation of cellular materials with target properties. These advancements underscore CM-Net's transformative potential as a universal tool for the next generation of cellular material design and optimization.

6 | Methods

We detail the dataset generation procedure, including methods for constructing TWSs and finite element model settings to assess their EA performance. We also describe the machine learning model architecture and training procedures.

6.1 | Design Generation

TWSs can be categorized based on the edge types of their axial cross-sectional shapes: straight or curved edges. For generating curved edges, we employed B-spline curves, while polylines were used for straight edges. These were defined by control points. The parametric function of a B–spline curve of order p with n control points is given by

$$S(\xi) = \sum_{i=0}^{n-1} P_i b_{i,p}(\xi) \tag{4}$$

where $S(\xi)$ signifies the curve, P_i represents the control points, and ξ denotes the parametric coordinate. The B-spline basis functions are defined by

$$b_{i,0}(\xi) = \begin{cases} 1, & \text{if } \xi_i \le \xi < \xi_{i+1} \\ 0, & \text{otherwise} \end{cases} \tag{5}$$

$$b_{i,p}(\xi) = \frac{\xi - \xi_i}{\xi_{i+p} - \xi_i} b_{i,p-1}(\xi) + \frac{\xi_{i+p+1} - \xi}{\xi_{i+p+1} - \xi_{i+1}} b_{i+1,p-1}(\xi) \quad \text{if } \xi_i \le \xi < \xi_{i+1} \tag{6}$$

with the convention that $0/0 = 0$. For this work, we set $p = 3$, $n = 11$, and the knot vector $[\xi_0, \xi_1, \ldots, \xi_{n+p}] = [0.0, 0.0, 0.0, 0.0, 0.125, 0.25, 0.375, 0.5, 0.625, 0.75, 0.875, 1.0, 1.0, 1.0, 1.0]$. The x and y coordinates of the B–spline curve are bound within [0.0, 0.5] and [−0.5, 0.5], respectively. Due to central symmetry and boundary constraints, only four control points were variable, with the 1st, 6th, and 11th control points fixed at (0.0, 0.0), (0.5, 0.0), and (1.0, 0.0), respectively. The number of polyline control points was selected as an even number between 4 and 14, with other settings matching those of B-spline curves. Both curves and polylines were validated during generation to prevent edge intersections. Using square and hexagonal cross-sections as baselines, we generated polyline square tubes, B-spline square tubes, B-spline hexagonal tubes, and B-spline hexagonal honeycombs. Wall thickness ranged from 0.2 to 0.6 mm, with cross-sectional basic lengths of 16.67 mm and heights fixed at 28 mm. To expand the topology types, we incorporated common TWSs from previous research, including triangular, square, hexagonal, and circular cross-sections. These had limited parameters, with thicknesses from 0.1 to 1.0 mm and unchanged basic length and height. The complete methodology is detailed in Section S1.1.

6.2 | Sample Fabrication

The experimental specimens were fabricated using wire-cut electrical discharge machining, which is particularly well suited for achieving high precision in the manufacturing of TWSs. The process began with the preparation of aluminum alloy AA1060-H112 blocks as base workpieces. Subsequently, holes were drilled at the centers of each structural cell to facilitate the threading of the wire during the machining process. The wire was threaded through each hole and guided along the internal contour of the TWSs. After completing the inner contour, the wire was repositioned outside the block and used to cut the outer profile of the TWSs.

6.3 | Finite Element Simulation

We employed LS-DYNA to obtain force–displacement responses of generated structures and Hypermesh for meshing, using Belytschko-Tsay shell elements. Mesh refinement continued until convergence was achieved, with sizes set at 0.7 mm for TWSs and 10 mm for rigid plates. Hourglass deformations were mitigated using stiffness-based hourglass control. Boundary conditions included fixing the bottom rigid plate and applying a vertical velocity of 1 mm/ms to the top plate to simulate quasi-static compression, ensuring kinetic energy did not exceed 1% of internal energy. The automatic node-to-surface contact was specified between TWSs and plates, with the automatic single surface contact applied to TWSs to prevent self-penetration. Friction coefficients were set at 0.2 for both static and dynamic conditions. The aluminum alloy material was modeled using a piecewise-linear plasticity model (MAT 24), with plastic properties defined by an equivalent stress-plastic strain curve. Vertical displacement of the upper plate and reaction forces between TWSs and the upper plate were recorded. The accuracy of this FEM was validated in our prior work [20]. Detailed parameters are provided in Section S1.2.

6.4 | Mechanical Testing

All quasi-static compression tests were performed using a universal testing machine, MTS 5944 (Instron Corporation). The samples are compressed between stationary and moving steel plates. To resemble the boundary conditions used in the training dataset, the samples are in free contact with the two plates. Force-displacement curves are measured by the load cell with a maximum capacity of 100 kN and the built-in crosshead encoder. Stress–strain curves are computed analogously to what is done for FE simulations. The compression velocity for all tests is set to 2.0 mm/min.

6.5 | EA Metrics

The EA metrics evaluated include the IPCF, MCF, EA, and specific energy absorption (SEA). IPCF reflects the initial buckling force, which is crucial for controlling acceleration imparted to protected objects. The total energy absorbed up to densification displacement δ_D is expressed as

$$EA = \int_0^{\delta_D} F(\delta) d\delta = MCF \cdot \delta_D \tag{7}$$

where $F(\delta)$ denotes the compression force at displacement δ. To determine δ_D, the EA efficiency (EAE) is denoted as

$$EAE(\delta) = \frac{\int_0^{\delta} F(\delta) d\delta}{F_{max} \cdot h} \tag{8}$$

δ_D corresponds to the displacement where EAE reaches its maximum value. In addition, F_{max} signifies the maximum force when the displacement ranges between 0 and δ. SEA, a parameter critical for assessing EA performance across different structures, is defined as

$$SEA = \frac{EA}{m} \tag{9}$$

where m is the mass of the structure.

6.6 | Architecture of CM-Net for TWSs

The architecture of CM-Net for TWSs is summarized below, with full technical details provided in our Code availability and supplementary materials. Implemented using TensorFlow, the network processes input basic geometric units containing numbers of repeated units, wall thicknesses, coordinate points, included angles, and material properties. Key operations include:

1. Coordinate point tensor duplication and reversal to generate forward and inverse edge representations.
2. Two three-layer neural networks processing included angle information: $(32 \to 32 \to 4)$ and $(32 \to 32 \to 6)$ for adjacent included angles, and other included angles, respectively, followed by a global sum pooling 1D layer for dimension reduction.
3. Concatenation of coordinate and angle tensors, processed through a shared trainable linear layer with 512 neurons, followed by summation and maximum operations to form a directionless geometric unit.
4. Wall thickness embedding via a trainable linear layer with 32 neurons, and material property processing using two three-layer networks $(32 \to 32 \to 1)$ and $(32 \to 32 \to 32)$ to obtain flow stress and high-dimensional embeddings of material parameters.
5. The procedure involving the application of an adjacency matrix to a user-defined layer and following a trainable linear layer with 16 neurons is repeated twice to gather constrained information.
6. A multi-head self-attention layer (with 2 attention heads, each of key dimension 8) and a trainable linear layer with 8 neurons capture global characteristics of structures, and these concatenated with prior features to form basic mechanical units.
7. After being processed by a two-layer perceptron $(1024 \to 1024)$ with a residual block, basic mechanical units are processed by different subnetworks to obtain PCF, MCF, and EA, respectively.

The details are introduced in Section S3.1 and S3.2.

6.7 | Training Protocol

The curved and straight edges of TWSs are represented by B-spline curves and straight lines, respectively. However, the representation of control points can be less intuitive during the design process. To facilitate a more user-friendly and interpretable design methodology, we adopt a representation based on edit points. Although restricting the number of edit points introduces some error in the curve representation, this trade-off is justified by the improvement in usability and design efficiency. In this study, the distribution of edit points is strategically determined based on the curvature distribution of the structure. Specifically, regions with higher curvature are assigned a greater number of edit points, thereby enabling more accurate representations in those critical areas. The code implementing the discretization of B-spline curves into 40 edit points based on curvature is provided in Code availability. For straight lines, the geometry can be precisely captured by specifying the coordinates of the two endpoints. To maintain consistency and simplify the input format, the starting point is always fixed at (0, 0), while the remaining 38 edit points are also set to (0, 0). The adjacency matrix serves as a critical input to the model, representing the connection relationships among the basic geometric units. It is important to note that a basic geometric unit may connect to the same unit as itself, and this must be explicitly included in the adjacency matrix. Detailed illustrations of how to construct these input matrices for the CM-Net are provided in Section S3.1.

To ensure numerical consistency and compatibility with the model, the adjacency matrix inputs are normalized by dividing the values by 10. The training hyperparameters employed in this study are detailed in Table S3, and loss plots are presented in Section S4. Due to its lightweight design, requiring about 4 million parameters for the original model and only 186 thousand parameters for the lightweight version, the CM-Net is highly deployable on standard computing hardware, such as personal computers or laptops. In this study, we trained the CM-Net on a PC equipped with an Nvidia GeForce RTX 4060 Ti GPU, which has 16 GB of GDDR6 memory. The training process for the original model took approximately 1.2 h. Further details regarding the training procedure and performance evaluation are described in Sections S4, S5.3, and S6.

6.8 | Finetune and Optimization

The dataset for fine-tuning CM-Net includes 170 square-boundary samples, 40 C-shaped boundary samples, 40 U-shaped boundary samples, 40 H-shaped boundary samples, and 40 K-shaped boundary samples, totaling 330 samples. These samples were randomly divided into training and validation sets in a 7:3 ratio. Notably, the weights in the mechanical property prediction module were set as trainable parameters, while all other weights were frozen. The lightweight version of CM-Net was selected as the base model, resulting in 25 800 trainable parameters. All other training settings followed the standard procedure. A genetic algorithm was employed in this study as the optimization algorithm, with the seeds and wall thickness of the Voronoi diagram serving as the genetic representation of the thin-walled structure. The algorithm incorporates two primary operators: the mutation operator and the insertion/deletion operator. The mutation operator modifies the coordinates of the seeds and the wall thickness values, with the seed coordinates constrained within the design boundary and the wall thickness ranging from 0.5 to 1.0 mm. This operator was applied with a probability of 20%. The insertion/deletion operator adjusts the number of seeds to generate

Voronoi diagrams with varying complexity levels, with the seed count constrained between 4 and 20. This operator was implemented with a 50% probability, with equal likelihood for both insertion and deletion operations. An elitist strategy was incorporated, where the top 10% of the population with the highest fitness values were preserved for the next generation. The population size was set to 50 individuals, and the algorithm was executed for 200 generations. The initial population was randomly generated, ensuring a diverse starting point for the evolutionary process. The design target was defined through a carefully formulated fitness function. To achieve maximum SEA while avoiding exceeding the limitations of protected items, both the IPCF and MCF needed to be controlled. Therefore, the fitness function can be defined by

$$F(\mathrm{IPCF}, \mathrm{MCF}, \mathrm{SEA}) = \mathrm{SEA} + k(\mathrm{ReLU}(\mathrm{IPCF} - \mathrm{IPCF_m}) + \mathrm{ReLU}(\mathrm{MCF} - \mathrm{MCF_m})) \tag{10}$$

where k represents the penalty coefficient, $\mathrm{IPCF_m}$ and $\mathrm{MCF_m}$ denote the maximum IPCF and MCF values, respectively. Both $\mathrm{IPCF_m}$ and $\mathrm{MCF_m}$ were set to 15 kN. The ReLU function is mathematically expressed as

$$\mathrm{ReLU}(x) = \begin{cases} x, & x > 0 \\ 0, & x \le 0 \end{cases} \tag{11}$$

Additionally, to ensure manufacturability through wire-cut electrical discharge machining, the minimum edge length in Voronoi tubes was specified as 2.0 mm.

6.9 | Error Measures

To measure the error between the ground truth and prediction, we consider the relative error computed as

$$\mathrm{RE}(y_{\mathrm{pred}}, y_{\mathrm{true}}) = \left| \frac{y_{\mathrm{pred}} - y_{\mathrm{true}}}{y_{\mathrm{true}}} \right| \times 100\% \tag{12}$$

where y_{pred} and y_{true} are the values predicted by CM-Net and the values obtained by FEM, respectively.

Acknowledgments

This work was supported by the Research Grants Council (Project nos.: C4074-22G, STG5/E-103/24-R, and SRFS2627-4S01), Hong Kong Special Administrative Region, China, and The Chinese University of Hong Kong (Project nos.: 3110174 and 4935121).

Funding

This study was supported by Research Grants Council (C4074-22G, STG5/E-103/24-R, and SRFS2627-4S01) and Chinese University of Hong Kong (3110174 and 4935121).

Code Availability

The code developed in this study is available via GitHub at https://github.com/sczhou-c/CM-Net.

Conflicts of Interest

The authors declare no conflicts of interest.

Data Availability Statement

All data are available in the main text or the supplementary materials. The database has been deposited on 4TU.ResearchData under accession code https://data.4tu.nl/datasets/e9b1ff9f-a3a9-40b3-a088-775e1bcaaa1e.

References

1. S. Zhou, H. Liu, B. Li, X. Yang, and J. Yang, "A Detachable Chain Tensile Energy Absorber Inspired by Mortise and Tenon Joint," *International Journal of Mechanical Sciences* 223 (2022): 107290.

2. Z. Zhuang, Z. Qian, X. Wang, et al., "Bioinspired Structural Composite Flexible Material With High Cushion Performance," *Advanced Science* 11 (2024): e2304947.

3. S. Zhou, H. Liu, J. Ma, X. Yang, and J. Yang, "Deformation Behaviors and Energy Absorption Characteristics of a Hollow Re-Entrant Auxetic Lattice Metamaterial," *Aerospace Science and Technology* 142 (2023): 108583.

4. J. Ding, Q. Ma, X. Li, et al., "Imperfection-Enabled Strengthening of Ultra-Lightweight Lattice Materials," *Advanced Science* 11 (2024): 2402727.

5. X. Fang, D. Yu, J. Wen, et al., "Large Recoverable Elastic Energy in Chiral Metamaterials via Twist Buckling," *Nature* 639 (2025): 639–645.

6. X. Yang, L. Cheng, H. Liu, S. Zhou, and J. Yang, "Chain Structure for Ceramic Lattices With Improved Energy Absorption and Delayed Failure," *International Journal of Engineering Science* 222 (2026): 104479.

7. P. Yin, B. Li, J. Hong, et al., "Design Criteria for Architected Materials With Programmable Mechanical Properties Within Theoretical Limit Ranges," *Advanced Science* 11 (2024): e2307279.

8. W. Liu, S. Janbaz, D. Dykstra, B. Ennis, and C. Coulais, "Harnessing Plasticity in Sequential Metamaterials for Ideal Shock Absorption," *Nature* 634 (2024): 842–847.

9. S. Zhou, L. Jin, G. Xie, K. Zhang, Q. Gao, and W.-H. Liao, "Thermally Driven Reusable Dual-Phase Honeycombs With Enhanced Mechanical Properties," *International Journal of Mechanical Sciences* 326 (2026): 111900.

10. Y. Xing, Z.-L. Zhao, L. Huang, and J. Yang, "A Self-Constrained Energy-Absorbing Structure With Robust Crashworthiness Inspired by Photonic Micropillars Pattern in Beetle's Elytra," *Composite Structures* 319 (2023): 117193.

11. X. Zheng, H. Lee, T. H. Weisgraber, et al., "Ultralight, Ultrastiff Mechanical Metamaterials," *Science* 344 (2014): 1373–1377.

12. J. Ding, Y. Wen, Q. Wang, S. Qu, X. Song, and B. Zhang, "Material-Gradient Enabled Enhancement of Strength and Strain-Hardening of Lattice Structures," *Advanced Science* 12 (2025): e11185.

13. T. Zhao, X. Dang, K. Manos, et al., "Modular Chiral Origami Metamaterials." *Nature* 640 (2025): 931–940.

14. Y. Li, W. Li, T. Han, et al., "Transforming Heat Transfer With Thermal Metamaterials and Devices," *Nature Reviews Materials* 6 (2021): 488–507.

15. A. Bergamini, M. Miniaci, T. Delpero, et al., "Tacticity in Chiral Phononic Crystals," *Nature Communications* 10, no. 1 (2019): 4525.

16. R. Yao, T. Pang, B. Zhang, J. Fang, Q. Li, and G. Sun, "On the Crashworthiness of ThIn-Walled Multi-Cell Structures and Materials: State of the Art and Prospects," *Thin-Walled Structures* 189 (2023): 110734.

17. W. W. S. Ma, H. Yang, Y. Zhao, et al., "Multi-Physical Lattice Metamaterials Enabled by Additive Manufacturing: Design Principles, Interaction Mechanisms, and Multifunctional Applications," *Advanced Science* 12 (2025): e2405835, https://doi.org/10.1002/advs.202405835.

18. P. Viveganathan, S. Gao, W. Ji, H. Fan, C. Han, and K. Zhou, "Recent Progress on 3D Printing of Lightweight Metal Thin-Walled Structures," *Advanced Materials* 36 (2024): e2402130.

19. K. Liu, R. Sun, and C. Daraio, "Growth Rules for Irregular Architected Materials With Programmable Properties," *Science* 377 (2022): 975–981.

20. S. Zhou, K. Zhang, L. Jin, Q. Gao, and W.-H. Liao, "Efficient Data Driven Optimization Framework for Designing B-Spline Honeycombs With Excellent Energy Absorption," *Thin-Walled Structures* 209 (2025): 112941.

21. Y. Yang, H. Liu, Q. Zhang, J. Ma, X. Yang, and J. Yang, "Energy Absorption Characteristics of a Super Hexagonal Honeycomb Under Out-of-Plane Crushing," *Thin-Walled Structures* 189 (2023): 110914.

22. A. Zolfagharian, L. Jin, Q. Ge, et al., "Roadmap on Artificial Intelligence-Augmented Additive Manufacturing," *Advanced Intelligent Systems* 8 (2026): e202500484.

23. K. A. Brown and G. X. Gu, "Computational Challenges in Additive Manufacturing for Metamaterials Design," *Nature Computational Science* 4 (2024): 553–555.

24. S. Bonfanti, S. Hiemer, R. Zulkarnain, R. Guerra, M. Zaiser, and S. Zapperi, "Computational Design of Mechanical Metamaterials," *Nature Computational Science* 4 (2024): 574–583.

25. H. Jin, B. Zhang, Q. Cao, et al., "Characterization and Inverse Design of Stochastic Mechanical Metamaterials Using Neural Operators," *Advanced Materials* 37 (2025): 2420063.

26. X. Q. Wang, Z. Jin, D. Ravichandran, and G. X. Gu, "Artificial Intelligence and Multiscale Modeling for Sustainable Biopolymers and Bioinspired Materials," *Advanced Materials* 37 (2025): 2416901.

27. A. E. Gongora, K. L. Snapp, R. Pang, et al., "Designing Lattices for Impact Protection Using Transfer Learning," *Matter* 5 (2022): 2829–2846.

28. S. Luan, E. Chen, J. John, and S. Gaitanaros, "A Data-Driven Framework for Structure-Property Correlation in Ordered and Disordered Cellular Metamaterials," *Science Advances* 9 (2023): eadi1453.

29. L. Zheng, D. M. Kochmann, and S. Kumar, "HyperCAN: Hypernetwork-Driven Deep Parameterized Constitutive Models for Metamaterials," *Extreme Mechanics Letters* 72 (2024): 102243.

30. H. Pahlavani, K. Tsifoutis-Kazolis, M. C. Saldivar, et al., "Deep Learning for Size-Agnostic Inverse Design of Random-Network 3D Printed Mechanical Metamaterials," *Advanced Materials* 36 (2024): e2303481.

31. S. Lee, Z. Zhang, and G. X. Gu, "Generative Machine Learning Algorithm for Lattice Structures With Superior Mechanical Properties," *Materials Horizons* 9 (2022): 952–960.

32. W. Deng, S. Kumar, A. Vallone, D. M. Kochmann, and J. R. Greer, "AI-Enabled Materials Design of Non-Periodic 3D Architectures With Predictable Direction-Dependent Elastic Properties," *Advanced Materials* 36 (2024): 2308149.

33. Z. Chai, Z. Zong, H. Yong, et al., "Tailoring Stress–strain Curves of Flexible Snapping Mechanical Metamaterial for on-Demand Mechanical Responses via Data-Driven Inverse Design," *Advanced Materials* 36 (2024): 2404369.

34. S. Kumar, S. Tan, L. Zheng, and D. M. Kochmann, "Inverse-Designed Spinodoid Metamaterials," *NPJ Computational Materials* 6 (2020): 1–10.

35. J.-H. Bastek, S. Kumar, B. Telgen, R. N. Glaesener, and D. M. Kochmann, "Inverting the Structure–property Map of Truss Metamaterials by Deep Learning," *Proceedings of the National Academy of Sciences* 119 (2022): e2111505119.

36. C. S. Ha, D. Yao, Z. Xu, et al., "Rapid Inverse Design of Metamaterials Based on Prescribed Mechanical Behavior Through Machine Learning," *Nature Communications* 14 (2023): 5765.

37. Y. Mao, Q. He, and X. Zhao, "Designing Complex Architectured Materials With Generative Adversarial Networks," *Science Advances* 6 (2020): eaaz4169.

38. J.-H. Bastek and D. M. Kochmann, "Inverse Design of Nonlinear Mechanical Metamaterials via Video Denoising Diffusion Models," *Nature Machine Intelligence* 5 (2023): 1466–1475.

39. A. K. Shargh and N. Abdolrahim, "An Interpretable Deep Learning Approach for Designing Nanoporous Silicon Nitride Membranes With Tunable Mechanical Properties," *NPJ Computational Materials* 9 (2023): 32.

40. Y. He, Y. Tan, M. Yang, et al., "Accurate Prediction of Discontinuous Crack Paths in Random Porous Media via a Generative Deep Learning Model," *Proceedings of the National Academy of Sciences* 121 (2024): e2413462121.

41. S. Zhou, H. Liu, D. Yang, et al., "Machine Learning for Predicting and Optimizing Energy Absorption Characteristics of Hollow Variable Cross-Section Lattice Metamaterials," *Thin-Walled Structures* 224 (2026): 114650.

42. B. Peng, Y. Wei, Y. Qin, et al., "Machine Learning-Enabled Constrained Multi-Objective Design of Architected Materials," *Nature Communications* 14 (2023): 6630.

43. Y. Jadhav, J. Berthel, C. Hu, R. Panat, J. Beuth, and A. Barati Farimani, "Generative Lattice Units With 3D Diffusion for Inverse Design: GLU3D," *Advanced Functional Materials* 34 (2024): 2404165.

44. X. Zheng, I. Watanabe, J. Paik, J. Li, X. Guo, and M. Naito, "Text-to-Microstructure Generation Using Generative Deep Learning," *Small* 20 (2024): 2402685.

45. Y. Liu, W. Huang, Z. Wang, J. Zhang, and J. Liu, "Machine Learning-Based Mechanical Performance Prediction and Design of Lattice Structures," *International Journal of Mechanical Sciences* 294 (2025): 110230.

46. L. Zheng, K. Karapiperis, S. Kumar, and D. M. Kochmann, "Unifying the Design Space and Optimizing Linear and Nonlinear Truss Metamaterials by Generative Modeling," *Nature Communications* 14 (2023): 7563.

47. I. Grega, I. Batatia, P. P. Indurkar, G. Csányi, S. Karlapati, and V. S. Deshpande, "Graph Neural Networks for Strut-Based Architected Solids," *Journal of the Mechanics and Physics of Solids* 195 (2025): 105966.

48. B. Jiang, Y. Wang, H. Niu, X. Cheng, P. Zhao, and J. Bao, "GNNs for Mechanical Properties Prediction of Strut-Based Lattice Structures," *International Journal of Mechanical Sciences* 269 (2024): 109082.

49. L. Xiao, G. Shi, and W. Song, "Machine Learning Predictions on the Compressive Stress–strain Response of Lattice-Based Metamaterials," *International Journal of Solids and Structures* 300 (2024): 112893.

50. OpenAI J. Achiam, S. Adler, S. Agarwal, et al., GPT-4 Technical Report. arXiv preprint arXiv:2303.08774. (2023), https://doi.org/10.48550/arXiv.2303.08774.

51. A. I. DeepSeek, D. Guo, D. Yang, et al., DeepSeek-R1: Incentivizing Reasoning Capability in LLMs via Reinforcement Learning, arXiv preprint arXiv:2501.12948. (2025), https://doi.org/10.48550/arXiv.2501.12948.

52. G. E. Karniadakis, I. G. Kevrekidis, L. Lu, P. Perdikaris, S. Wang, and L. Yang, "Physics-Informed Machine Learning," *Nature Reviews Physics* 3 (2021): 422–440.

53. J. Yu, Z. Li, G. Chen, et al., "Computing the Relative Binding Affinity of Ligands Based on a Pairwise Binding Comparison Network," *Nature Computational Science* 3 (2023): 860–872.

54. D. Raabe, J. R. Mianroodi, and J. Neugebauer, "Accelerating the Design of Compositionally Complex Materials via Physics-Informed Artificial Intelligence," *Nature Computational Science* 3 (2023): 198–209.

55. Y. Wang, D. Jin, J. Chen, and X. Bai, "Revelation of Hidden 2D Atmospheric Turbulence Strength Fields From Turbulence Effects in Infrared Imaging," *Nature Computational Science* 3 (2023): 687–699.

56. Y. Tang, G. Li, T. Zhang, et al., "Digital Channel-Enabled Distributed Force Decoding via Small Datasets for Hand-Centric Interactions," *Science Advances* 11 (2025): eadt2641.

57. L. Pottier, A. Thorin, and F. Chinesta, "Latent-Energy-Based NNs: An Interpretable Neural Network Architecture for Model-Order Reduction of

Nonlinear Statics in Solid Mechanics," *Journal of the Mechanics and Physics of Solids* 194 (2025): 105953.

58. J. Sun, Y. He, X. Zhang, X. Li, M. Lu, and Y. Chen, "Energy Absorption and Topology Optimization of Self-Similar Inspired Multi-Cell Square Tubes," *Thin-Walled Structures* 196 (2024): 111491.

59. S. Tabacu, "Axial Crushing of Circular Structures With Rectangular Multi-Cell Insert," *Thin-Walled Structures* 95 (2015): 297–309.

60. M. Zaheer, S. Kottur, S. Ravanbakhsh, et al., "Deep Sets," in *Advances in Neural Information Processing Systems* (Curran Associates, Inc, 2017), Vol. 30.

61. R. Q. Charles, H. Su, M. Kaichun, and L. J. Guibas, "PointNet: Deep Learning on Point Sets for 3D Classification and Segmentation," in 2017 IEEE Conference on Computer Vision and Pattern Recognition (CVPR). (IEEE, 2017), 77-85. https://doi.org/10.1109/CVPR.2017.16.

62. J. Lee, Y. Lee, J. Kim, et al., "Set Transformer: A Framework for Attention-based Permutation-Invariant Neural Networks," in Proceedings of the 36th International Conference on Machine Learning, (PMLR, 2019), 3744–3753.

63. M. Maurizi, D. Xu, Y.-T. Wang, et al., "Designing Metamaterials With Programmable Nonlinear Responses and Geometric Constraints in Graph Space," *Nature Machine Intelligence* 7 (2025): 1023–1036.

64. Z. Wei, J. Chen, and K. Wei, "Generative Deep Learning for Designing Irregular Metamaterials With Programmable Nonlinear Mechanical Responses," *International Journal of Mechanical Sciences* 291-292 (2025): 110123–110292.

65. K. Karapiperis and D. M. Kochmann, "Prediction and Control of Fracture Paths in Disordered Architected Materials Using Graph Neural Networks," *Communications Engineering* 2 (2023): 32.

66. W. Cai, J. Jiang, F. Wang, J. Tang, S. Kim, and J. Huang, "A Survey on Mixture of Experts in Large Language Models," *IEEE Transactions on Knowledge and Data Engineering* 37, no. 7 (2025): 3896–3915, https://doi.org/10.1109/TKDE.2025.3554028.

Supporting Information

Additional supporting information can be found online in the Supporting Information section.